

PolarMOT: How Far Can Geometric Relations Take Us in 3D Multi-Object Tracking?

Aleksandr Kim, Guillem Brasó, Aljoša Ošep, and Laura Leal-Taixé

Technical University of Munich, Germany

{aleksandr.kim, guillem.braso, aljosa.osep, leal.taixe}@tum.de

Abstract. Most (3D) multi-object tracking methods rely on appearance-based cues for data association. By contrast, we investigate *how far we can get* by only encoding geometric relationships between objects in 3D space as cues for data-driven data association. We encode 3D detections as nodes in a graph, where spatial and temporal pairwise relations among objects are encoded via *localized polar* coordinates on graph edges. This representation makes our geometric relations invariant to global transformations and smooth trajectory changes, especially under non-holonomic motion. This allows our graph neural network to learn to effectively encode *temporal and spatial* interactions and fully leverage contextual and motion cues to obtain final scene interpretation by posing data association as edge classification. We establish a new state-of-the-art on nuScenes dataset and, more importantly, show that our method, *PolarMOT*, generalizes remarkably well across different locations (Boston, Singapore, Karlsruhe) and datasets (nuScenes and KITTI).

Keywords: 3D multi-object tracking, graph neural networks, lidar scene understanding

1 Introduction

Intelligent agents such as autonomous vehicles need to understand dynamic objects in their surroundings to safely navigate the world. 3D multi-object tracking (MOT) is, therefore, an essential component of autonomous intelligent systems.

State-of-the-art methods leverage the representational power of neural networks to learn appearance models [57,64] or regress velocity vectors [62] as cues for data association. While powerful, such methods need to be trained for the specific environments in which they are deployed. Methods such as [56,9] rely on motion as the key cue for association and can thus generalize across different environments. However, performance-wise they lag behind data-driven methods as they treat individual objects in isolation and do not consider their interactions.

In this work, we investigate *how far we can get* by learning to track objects given *only geometric cues* in the form relative pose differences between 3D bounding boxes *without* relying on any appearance information. This approach is not coupled to any specific object detector, sensor modality, or region-specific

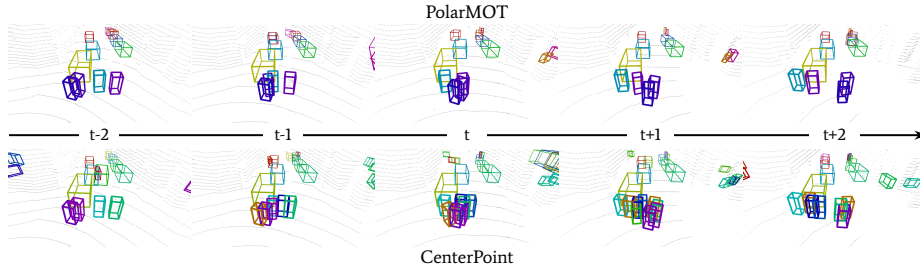


Fig. 1: *PolarMOT* tracks objects in 3D (offline and online) using a graph neural network that learns to associate 3D bounding boxes over time solely based on their relative geometric features and spatio-temporal relationships. Considering such object interactions improves *PolarMOT*'s ability to handle scenarios with high occlusions (pedestrian crossing) compared to others, *e.g.* CenterPoint.

appearance models. Consequentially, it generalizes well across different environments and geographic locations, as we experimentally demonstrate. By contrast to prior work [56] that rely on individual object motion as the main association cue, our method can learn how objects move as a group, taking into account their interactions to better adapt to dynamic environments and crowded scenarios.

As graphs are a natural representation for such long-term agent interactions, we represent our scene as a *sparse, multiplex* graph, which is then processed by a graph neural network (Fig. 2). We encode 3D detection as nodes, while edges represent their *spatial* and *temporal* relations and denote possible associations and influences. After several message passing steps in this graph, our neural network outputs binary classifications for all *temporal* edges. All nodes connected with a positive edge form a track and thus get assigned a consistent track ID [5].

One of our main insights is that encoding pairwise geometric relations, *i.e.*, edge features, in *localized polar* instead of Cartesian space is the key to good generalization and robustness and enables our model to effectively learn to track by *solely* relying on geometric cues. The pair-specific nature of the features makes them invariant to global transforms. Thus, features encoding relations between different detections of an object that moves consistently will be *stable*, regardless of the route geometry or point of reference. Such polar representation also naturally encodes non-holonomic motion prior, *i.e.*, a motion that is constrained by heading direction and is well parametrized by heading angle and velocity.

We evaluate our method, *PolarMOT*, on KITTI [13] and nuScenes datasets [8]. Our ablations reveal that our proposed graph structure and edge feature parametrization are pivotal for our final model achieving 66.4 average AMOTA, setting a new state-of-the-art on nuScenes MOT dataset among lidar-based methods. More importantly, we show that our learned tracker, which relies only on geometry leads to strong generalization across different geographic regions (Boston, Singapore, Karlsruhe) and datasets (nuScenes, KITTI), without fine-tuning. We are not suggesting to *not use* appearance cues, but point out that we can get very far with a minimalistic, graph-based tracking, solely relying on geometric cues and inferring object properties implicitly from interactions.

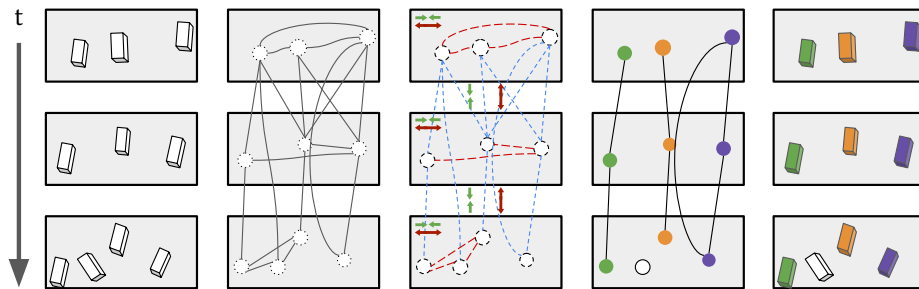


Fig. 2: Given a set of 3D bounding boxes in a sequence, *PolarMOT* constructs a graph encoding detections as nodes, and their geometric relations as *spatial* and *temporal* edges. After refining edge features via message passing with wider spatial and temporal context, we classify edges to obtain object track predictions.

To **summarize**, (i) we propose a minimalistic, graph-based 3D tracker that relies only on geometric cues and, without any bells and whistles or image/lidar input, establish new state-of-the-art on the nuScenes dataset; (ii) we suggest a graph-based representation of the scene that encodes temporal and spatial relations via a localized polar representation. This is not only to achieve state-of-the-art performance on benchmarks but, more importantly, is the key to strong generalization; (iii) as efficiency and online operation are crucial for robotic/AV scenarios, we construct a sparse graph and only establish links that are feasible based on maximal possible velocity and show how such sparse graphs can be constructed in an online fashion. We hope our code and models, available at [polar-mot.github.io](https://github.com/polar-mot/polar-mot), will run on friendly future robots!

2 Related Work

This section reviews relevant related work in 2D and 3D multi-object tracking (MOT) based on the well-established *tracking-by-detection* paradigm.

2D MOT. Early methods for vision-based MOT rely on hand-crafted appearance models [33,10] and motion cues [33,23], in conjunction with optimization frameworks for data association that go beyond simple bi-partite matching [20]. These include quadratic pseudo-boolean optimization [25], graph-based methods [41,46,65,7,6], conditional random fields [33,10] and lifted multi-cuts [51]. Orthogonally, the community has also been investigating lifting data association from image projective space to 3D via depth maps [25,24,38,39,30,47].

In the era of deep learning, the community has been focusing on learning strong appearance models [22,55,50], future target locations [2,60] or predicting offset vectors as cues for association [66]. Recently, we have witnessed a resurgence in graph-based approaches for tracking. MPNTrack [5] encodes 2D object detections as nodes while edges represent possible associations among them. Then, a message passing [14] graph neural network (GNN) [15] is used to update node/edge representation with temporal context, as needed for reliable

binary edge classification to obtain final tracks. Just as [5], we (i) encode detections as nodes, while edges represent hypothetical associations, and we (ii) learn to classify edges to obtain the final set of tracks. Different to [5], we tackle 3D MOT using *only* geometric cues. Our model encodes both, temporal and spatial relations and, importantly, encodes them via *localized polar coordinates*, that encode non-holonomic motion prior. Moreover, beyond *offline* use-case, we show how to construct *sparse* graphs in *online* fashion, as needed in mobile robotics.

3D MOT. Early methods for 3D detection and tracking [11,40] model vehicles as cuboids or rely on bottom-up point cloud segmentation [52,34,16] and track objects using (extended) Kalman filter. Thanks to developments in deep point-based representation learning [43,44,53,67], we nowadays have strong backbones, as needed for 3D object detection [42,48,67,61,21,62], tracking [12,56,9] and segmentation [1]. AB3DMOT [56] shows that well-localized lidar-based 3D object detections work very well in conjunction with a simple Kalman filter based tracking framework [4]. Association can be performed based on 3D bounding box overlap or centroid-based Mahalanobis distance [9] to increase robustness to lower frame rates. State-of-the-art CenterPoint [62] learns to detect objects as points and regresses velocity vectors needed for the association. Similar to ours, OGR3MOT[63] also tackles 3D MOT using message passing networks based framework, proposed by [5]. However, it represents detections *and* tracks as two distinct types of nodes, thus effectively maintaining two subgraphs. *Different* to that, *our PolarMOT* implicitly derives node embeddings from relational (edge) features parametrized via proposed local polar coordinates. A recent body of work proposes to fuse image and lidar data [17,64,57]. GNN3DMOT [57] utilizes GNNs to learn appearance and motion features for data association jointly. This approach relies on Hungarian algorithm to perform data association based on the learned features. *Different* to that, we *only* use 3D geometric cues and perform association directly via edge classification in end-to-end manner.

3 Message Passing Networks for Multi-Object Tracking

Our work is inspired by MPNTrack [5], an image-based MOT method that we summarize for completeness. MPNTrack models detections as graph nodes and represents possible associations via edges. After propagating features via neural message passing [14], edges are classified as active/inactive.

MPNTrack processes a clip of frames with detected objects, and outputs classifications of links between them. For each clip, input is a set of object detections $\mathcal{O} = \{o_i\}_{i=1}^n$, represented via an (appearance) embedding vector, 2D position and timestamp. Then, a graph $G = (V, E)$ where $V = \mathcal{O}$ and $E \subset \mathcal{O} \times \mathcal{O}$. MPNTrack encodes only inter-frame edges and heuristically prunes them for sparsity. Each node $o_i \in V$ and edge $e_{ij} \in E$ (connecting o_i, o_j) have corresponding initial embeddings $h_i^{(0)}$ and $h_{(i,j)}^{(0)}$ obtained from appearance and position cues. These embeddings are propagated across the graph via neural message passing for a fixed number of iterations L to obtain updated edge features $h_{(i,j)}^{(1,\dots,L)}$.

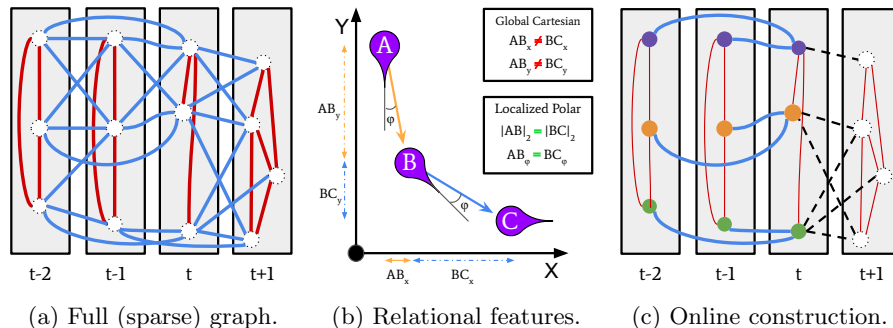


Fig. 3: The key contributions of our work: multiplex input graph with *inter-frame (temporal)* and *intra-frame (spatial)* edges, relative geometric features in localized polar coordinates and continuously evolving online graph construction.

More specifically, edge embeddings are updated at each message passing step based on embeddings from the previous step of the edge itself and its neighboring nodes. Nodes are then updated based on previous embeddings of the node and neighboring edges, which are aggregated separately for forward and backward directions in time. After L message passing updates, edges are classified based on their embeddings from all steps, $h_{(i,j)}^{(1,\dots,L)}$, where positive classification implies that two connected detections are part of the same track (identity).

4 PolarMOT

In this section, we provide a high-level overview of our *PolarMOT*, followed by a detailed discussion of our key ideas and components.

4.1 Method Overview

PolarMOT encodes the overall geometric configuration of detected objects and the relative pose changes between them as primary cues for tracking.

Sparse graph-based scene representation. We use a graph to represent object detections as nodes, and their geometric relations as edges. We encode both *temporal* and *spatial* relations among objects in two levels of our *sparse multiplex* graph (Fig. 3a). The *temporal* level connects nodes across different frames with *inter-frame edges*, while the *spatial* level connects nodes of the same frame with *intra-frame edges*. For sparsity, we *only* link nodes that are mutually reachable based on the maximal velocity of their semantic class.

Localized relational polar encoding We encode geometric relations among nodes via a localized polar-based representation (Fig. 3b). Our parametrization is not based on a shared global coordinate frame but is specific to each pair’s local frame. This makes our parametrization *invariant* to the reference world frame, and induces a *non-holonomic* (directional) motion prior.

Learning representation via message passing. We follow a message passing procedure [14] to iteratively update our features through alternating edge/node updates (Fig. 2, *center*). Node features are not extracted from input detections. Instead, they are learned *implicitly* through mutual object interactions.

Edge classification. To obtain object tracks, we classify our *temporal* edges using a multi-layer perceptron based on final edge representations (Fig. 2, *right*).

Online graph construction. For *online* tracking, we continuously evolve our input graph after each frame, while maintaining both sparsity and high connectivity (Fig. 3c). For online processing, we connect past track predictions directly to the most recent detections, thus allowing our network to infer historical context effectively via message passing on the graph topology.

4.2 Message Passing on a Sparse Multiplex Graph

Representation. Following [5], we represent each individual object detection as a *node* of the graph with *edges* encoding relations between objects. More precisely, we model *temporal* and *spatial* relations between objects (graph nodes) by encoding our 3D detections via a *sparse*, undirected *multiplex* graph with two distinct levels / edge types (Fig. 3a). In the *first level* we model temporal connections via undirected *inter-frame* edges between nodes across frames [5], which describe potential motion of objects. Each edge connects two distinct detections across frames. The edge features denote the likelihood of an object moving from pose/node A to pose/node B in the elapsed time. In the *second level*, we introduce undirected *intra-frame* edges (*i.e.*, links between nearby detections from the same frame) to model spatial context. These edges act as pathways to exchange frame-specific context and are meant to express the mutual influence of moving targets’ motion patterns. This should intuitively help with difficult and ambiguous cases that arise in crowded scenarios. Both inter- and intra-frame edges connect the same set of nodes, but convey semantically different information, effectively turning our graph into a multiplex network with two distinct levels. *Intra-frame* edges are excluded from edge classification.

Sparse graph construction. To handle occlusions, we connect nodes across any number of frames. Doing this naively would potentially result in a prohibitively dense graph. To ensure graph sparsity, we take full advantage of the 3D domain, and rely on physical constraints to establish only *relevant*, physically-plausible spatial or temporal relations. For *inter-frame edges*, if the physical distance between two detections is greater than the maximal velocity of the detected class, we consider it impossible for them to belong to the same object and do not form an edge. For *intra-frame edges*, we allow distance up to twice the maximal velocity to connect objects that could collide in the next frame if moving towards each other and, therefore, influence each other’s movement.

Message passing. Following the general message passing framework, our model performs a fixed number of alternating *edge* and *node* updates to obtain enhanced node/edge representation, as needed for edge classification.

Edge update: At every message passing iteration $l = 1, \dots, L$, we first update edge embeddings by learning to fuse the edge and connected node embeddings from the previous message passing iteration. More precisely, we update edge embedding $h_{(i,j)}$ between nodes o_i and o_j as follows:

$$h_{(i,j)}^{(l)} = \text{MLP}_{\text{edge}} \left(\left[h_i^{(l-1)}, h_{(i,j)}^{(l-1)}, h_j^{(l-1)} \right] \right). \quad (1)$$

During each update, the edge embedding from the previous message passing iteration $l - 1$, *i.e.*, $h_{(i,j)}^{(l-1)}$, is concatenated with embeddings $(h_i^{(l-1)}, h_j^{(l-1)})$ of the connected nodes. The result is then fused by MLP_{edge} , a Multi-Layer Perceptron (MLP), which produces the fused edge features $h_{(i,j)}^{(l)}$ (Eq. 1). This edge embedding update is identical for all edge types and directions.

Node update: To update nodes, first, we construct messages for each edge $h_{(i,j)}^{(l)}$ via learned fusion of *its updated edge* and *neighboring nodes'* features:

$$m_{(i,j)}^{(l)} = \begin{cases} \text{MLP}_{\text{past}} \left([h_i^{(l-1)}, h_{(i,j)}^{(l)}, h_j^{(l-1)}] \right) & \text{if } t_j < t_i, \\ \text{MLP}_{\text{pres}} \left([h_i^{(l-1)}, h_{(i,j)}^{(l)}, h_j^{(l-1)}] \right) & \text{if } t_i = t_j, \\ \text{MLP}_{\text{fut}} \left([h_i^{(l-1)}, h_{(i,j)}^{(l)}, h_j^{(l-1)}] \right) & \text{if } t_j > t_i. \end{cases} \quad (2)$$

Via *inter-frame edges* we produce two messages for each temporal direction: we produce *past* features via MLP_{past} and *future* features via MLP_{fut} (only in offline tracking settings). At the same time, we produce *present* features via MLP_{pres} for each *intra-frame*, spatial, edge. Using separate MLPs allows our model to learn different embeddings for each type of relationship.

Node aggregation: Then, each node $h_i^{(l)}$ *aggregates* incoming messages using an element-wise max operator, separately for past, present and future edges to maintain contextual awareness. The resulting aggregated vectors are concatenated and fused via MLP_{node} :

$$h_i^{(l)} = \text{MLP}_{\text{node}} \left(\left[\max_{t_j < t_i} m_{(i,j)}^{(l)}, \max_{t_i = t_j} m_{(i,j)}^{(l)}, \max_{t_j > t_i} m_{(i,j)}^{(l)} \right] \right). \quad (3)$$

As we do not use any object-specific information (*e.g.* appearance), we rely on the model to implicitly learn node features from their interactions.

Initialization: We *initialize* edge embeddings with relational features (as detailed in Sec. 4.3) processed by $\text{MLP}_{\text{edge-init}}$ (Eq. 4). These are then directly aggregated to produce *initial node embeddings* via $\text{MLP}_{\text{node-init}}$ (Eq. 5):

$$\text{(initial edge)} \quad h_{(i,j)}^{(1)} = \text{MLP}_{\text{edge-init}} \left(h_{(i,j)}^{(0)} \right), \quad (4)$$

$$\text{(initial node)} \quad h_i^{(1)} = \text{MLP}_{\text{node-init}} \left(\left[\max_{t_j < t_i} h_{(i,j)}^{(1)}, \max_{t_i = t_j} h_{(i,j)}^{(1)}, \max_{t_j > t_i} h_{(i,j)}^{(1)} \right] \right). \quad (5)$$

Tracking via edge classification. After graph construction and message passing, we classify *inter-frame* edges, which encode *temporal* relations. Positive classification implies the same object identity for both detections (*i.e.*, a consistent track ID). Any edge connecting nodes of the same track should be labeled as positive, regardless of the time difference between the connected nodes.

4.3 Localized Relational Polar Encoding

Depth sensors do not provide comparatively rich appearance information as images; however, they do provide accurate distance measurements to objects. Therefore, we fully focus on efficiently representing relative poses via edge features and learn node features implicitly. This leads to the question of how to represent geometric relations between objects efficiently? We start by representing each 3D detection as an oriented point with two planar coordinates x, y and orientation ϕ around vertical axis z , as differences in elevation, tilt, and spatial dimensions are insignificant between objects of the same class.

Global Cartesian coordinates. Traditionally, spatial geometric relations between objects are parametrized in Cartesian coordinates relative to some reference frame, encoding an edge $h_{i,j}^{(0)}$ connecting nodes o_i and o_j as:

$$h_{i,j}^{(0)} = \Delta(o_i, o_j) = \begin{bmatrix} \Delta x \\ \Delta y \\ \dots \end{bmatrix} = \begin{bmatrix} o_i^x - o_j^x \\ o_i^y - o_j^y \\ \dots \end{bmatrix}. \quad (6)$$

As shown in Fig. 3b, for *identical* pose changes \overrightarrow{AB} and \overrightarrow{BC} , global Cartesian features are *not identical*, as they depend on the orientation of the reference frame. *Identical motion non-intuitively leads to different relational features.*

Localized polar coordinates. We propose a different representation, which depends (i) only on the relevant pair of objects, o_i and o_j , and (ii) is more suitable for encoding directional non-holonomic motion. Our parametrization (Fig. 3b) expresses differences in poses A and B through a velocity vector, expressed in *polar coordinates*, where the center of the first detection A is the *pole* (*i.e.*, the origin of the polar coordinate frame), and its heading direction (downward) is the *polar axis*. This vector includes two components: *velocity* $|AB|$ (*i.e.*, distance between objects by detection time difference), and *polar angle* φ , *i.e.*, the angle between \overrightarrow{AB} and the polar axis of A (downward vector). We also include differences in object orientation (o^ϕ) and detection time difference (o^t):

$$h_{i,j}^{(0)} = \Delta(o_i, o_j) = \begin{bmatrix} v \\ \varphi_{i,j} \\ \Delta\phi \\ \Delta t \end{bmatrix} = \begin{bmatrix} \frac{\|o_i - o_j\|_2}{\Delta t} \\ \angle(\vec{o}_i^{head}, \vec{o}_j - \vec{o}_i) \\ o_i^\phi - o_j^\phi \\ o_i^t - o_j^t \end{bmatrix}. \quad (7)$$

We remove the dependency on an arbitrary reference frame by computing each feature relative to individual localized frames. *Now, identical motion between \overrightarrow{AB} and \overrightarrow{BC} leads to identical feature representation.*

Polar coordinates explicitly encode the change in heading angle (φ). This intuitively encodes a *smooth, non-holonomic* motion prior. For example, polar features for trajectory \overrightarrow{KL} and an (improbable) trajectory \overrightarrow{MN} significantly differ, while their Cartesian coordinates do not. These key characteristics allow *PolarMOT* to generalize well even when trained with a small number of labeled samples (Sec. 5.4), especially important for rarely observed object classes.

Table 1: Results of state-of-the-art methods for 3D multi-object tracking on the NuScenes test set. Legend: L – lidar, B – 3D bounding boxes

Method name	Input modality	IDs ↓ total	Recall ↑ average	AMOTA ↑ average	class-specific AMOTA ↑						
					car	ped	bicycle	bus	motor	trailer	truck
Ours	3D (B)	242	70.2	66.4	85.3	80.6	34.9	70.8	65.6	67.3	60.2
OGR3MOT [63]	3D (B)	288	69.2	65.6	81.6	78.7	38.0	71.1	64.0	67.1	59.0
CenterPoint [62]	3D (L)	684	68.0	65.0	81.8	78.0	33.1	71.5	58.7	69.3	62.5
IPRL-TRI [9]	3D (B)	950	60.0	55.0	71.9	74.5	25.5	64.1	48.1	49.5	51.3
AlphaTrack[64]	3D + 2D	718	72.3	69.3	84.2	74.3	47.1	72.0	72.8	72.0	62.6
EagerMOT [17]	3D + 2D	1156	72.7	67.7	81.0	74.4	58.3	74.0	62.5	63.6	59.7

Table 2: Online vs. offline tracking on the nuScenes validation set [8]

Method name	Input modality	IDs ↓ total	Recall ↑ average	AMOTA ↑ average	class-specific AMOTA ↑						
					car	ped	bicycle	bus	motor	trailer	truck
Ours <i>offl.</i>	3D	213	75.14	71.14	85.83	81.70	54.10	87.36	72.32	48.67	68.03
Ours <i>onl.</i>	3D	439	72.46	67.27	81.26	78.79	49.38	82.76	67.19	45.80	65.70
CenterPoint <i>onl.</i>	3D	562	70.62	65.91	84.23	77.29	43.70	80.16	59.16	51.47	65.39

4.4 Online Graph Construction

In this section, we propose an online graph construction approach that makes our method applicable to *online* applications. We maintain a *single* input graph for the whole sequence, which we continuously evolve with each incoming frame. This construction is identical to the *offline* setting, as discussed in Sec. 4.2. In each frame, edges are classified based on past-frame information *only*. There are multiple ways of maintaining a single input graph over a sequence of frames.

MPNTrack++: dense. First approach is a simple extension of prior offline GNN methods [5,26], where previous track associations do not influence the graph structure. At each frame, new nodes and edges are added to a continuously growing *dense* graph. *Such model is unaware of past track estimates.*

Prune inactive: consecutive. Past track estimates are a valuable cue that could be leveraged to resolve ambiguous associations. To this end, [63] propose to simply prune all past (negative) edges. This option encodes track history and maintains sparsity and due to frame-by-frame processing, preserved track edges always connect temporally *consecutive* nodes in each track. However, over time, the temporal distance from the current frame to early track nodes is increasing, making them unreachable within a limited number of message passing iterations. *This approach thus has a limited temporal receptive field.*

Ours: prune + skip. We propose a simple solution, that retains graph sparsity and provides global temporal receptive field from each newly-added node. After each frame, we remove all *past negative* edges *and* ensure we have, for each track, an edge between *each* most-recent track node and *all* past nodes from its track, see Fig. 3c. Moreover, new nodes (detections) at each frame are *only* connected to the most-recent track node for each existing track. By continuously evolving the graph in this manner we maintain sparsity, provide previous tracking decisions to the model through the input graph topology (this makes our model

Table 3: Ablation on parametrization of geometric relations among objects on nuScenes validation set. Trained on the **official mini** training set

Localized polar	Normalized by time	IDs ↓ total	Recall ↑ average	AMOTA ↑ average	class-specific AMOTA ↑						
					car	ped	bicycle	bus	motor	trailer	truck
✓	✓	430	62.12	57.96	85.16	80.80	44.02	80.68	45.83	5.41	63.83
✓	✗	652	55.07	52.17	81.51	80.14	06.66	79.53	53.82	0	63.51
✗	✓	1321	41.06	40.41	78.77	78.80	0	67.62	0	0	57.66

autoregressive) and keep all nodes reachable during message passing: any two connected nodes have at most two edges between them. *This allows our model to learn historical context directly via message passing to make well-informed edge classification, as needed for long-term tracking.*

4.5 Implementation details

Network structure. In *PolarMOT*, we use only fully connected (FC) layers with the leaky ReLU [36] nonlinearity, and the dimensionality of the edge and node features is 16 and 32 respectively. Our MLP_{node} and $\text{MLP}_{node.init}$ consist of 3 FC layers. Remaining MLPs consist of 2 layers with 70k parameters in total.

Training and augmentation. We train *PolarMOT* only on keyframes from the nuScenes [8] dataset, which we augment with noise dropout to mimic real detection performance. To mimic occlusions and false negatives, we randomly drop full frames, individual bounding boxes, and edges. To mimic false positives, we randomly add bounding boxes. We also perturb boxes by adding Gaussian noise to 3D positions and orientation. We train *PolarMOT* with focal loss [27], which is well suited for our imbalanced binary classification case. We use Radam optimizer [28,19] using cosine annealing with warm restarts [29] for 180 epochs with batch size of 64. For more details, we refer to the supplementary.

5 Experimental Evaluation

This section outlines our evaluation setting: datasets, metrics and input detections (Sec. 5.1). Next, in Sec. 5.2, we discuss our *offline* tracking results on the nuScenes test set and *online* and *offline* performance on the validation set, compared to the current state-of-the-art. Then, we justify our design decisions and discuss the benefits of our contributions via thorough ablation studies (Sec. 5.3). Finally, we demonstrate the generalization capabilities of *PolarMOT* by successfully applying it to different datasets and locations without fine-tuning (Sec. 5.4).

5.1 Evaluation setting

Datasets. We evaluate our method on nuScenes [8] and KITTI [13] tracking datasets. NuScenes was recorded in four locations across two cities: Boston, USA,

and Singapore. It contains 150 scenes, recorded with a 32-beam lidar sensor, and provides two scans per second (2Hz). KITTI tracking dataset was recorded in Karlsruhe, Germany, using a 64-beam lidar sensor at a 10Hz frame rate. Unless otherwise specified, we follow the official train/validation/test splits.

Evaluation metric. On the nuScenes dataset, we follow the official evaluation protocol that reports per-class and average AMOTA [56], which averages the CLEAR-MOT [3] MOTA metric across different recall thresholds. On KITTI, we also report sAMOTA [56] and HOTA [31] metrics, which allows us to analyze detection and association errors separately. We also report the number of identity switches (IDs) at the best performing recall. In the supplementary, we provide extended tables and evaluations that we omitted for brevity.

Object detections. On nuScenes, for a fair comparison with CenterPoint [62], we use their provided 3D detections (without the estimated velocity vectors). On KITTI, we use PointGNN [49] detections provided by EagerMOT [17].

5.2 Benchmark results

We compare our method to state-of-the-art 3D MOT on the official nuScenes benchmark. In Tab. 1 (*top*) we compare methods that rely *only* on the 3D input. As can be seen, our model ranks highest overall (66.4 avg. AMOTA compared to 2nd best 65.6). Our method only lags behind methods that additionally rely on rich visual signal (AlphaTrack and EagerMOT). While our focus was on effectively leveraging geometric relations, this hints that our approach could potentially further benefit from sensor fusion, which we leave for future work.

Online tracking. To confirm that our approach successfully handles online scenarios, we evaluate it on the nuScenes validation set with streaming inputs. In Tab. 2 we compare our *offline* and *online* versions, and compare both to *online* state-of-the-art CenterPoint [62] using the same 3D detections for all.

Not surprisingly, our *offline* model achieves the top performance at 71.14 avg. AMOTA. When switching to *online* inference, we achieve 67.27 avg. AMOTA (−3.87), outperforming CenterPoint by +1.36 avg AMOTA (from 65.91). As expected, there is a noticeable difference between our *offline* and *online* variants, as the online version is effectively exposed to only half of the context available to its offline counterpart, which observes both past and future detections.

5.3 Model ablation

Edge parametrization. To measure the impact of our proposed representation of geometric relations, we train three models with different relative feature parametrizations. The main advantage of our *proposed polar* representation is in the inductive bias that helps the model better understand long trajectories and non-holonomic motion. We conduct this experiment in the low data regime using the official nuScenes mini-split (1% of training data) and evaluate them on the (non-overlapping) validation set (150 seq.) and report results in Tab. 3.

Table 4: Ablation for intra-frame edges on the nuScenes validation set

Intra-frame connections	IDs ↓ total	Recall ↑ average	AMOTA ↑ average	class-specific AMOTA ↑						
				car	ped	bicycle	bus	motorcycle	trailer	truck
✓	213	75.14	71.14	85.83	81.70	54.10	87.36	72.32	48.67	68.03
✗	198	72.74	70.09	85.44	80.51	52.88	86.78	69.87	46.61	68.54

Table 5: Sparse graph construction: the impact of reducing/increasing the maximal velocity threshold on online tracking (nuScenes validation set)

Max edge distance	IDs ↓ total	Recall ↑ average	AMOTP ↓ average	AMOTA ↑ car	class-specific AMOTA ↑						
					ped	bicycle	bus	motorcycle	trailer	truck	
0.5x	1123	65.14	0.718	58.61	76.90	46.66	46.89	77.35	62.73	40.09	59.63
1.0x	439	72.46	0.595	67.27	81.26	78.79	49.38	82.76	67.19	45.80	65.70
2.0x	467	69.74	0.642	65.42	81.28	72.15	46.84	83.45	63.57	44.94	65.70

First row reports results obtained with our proposed model (time-normalized localized polar parametrization, together with orientation and time difference, as explained in Sec. 4.3). This approach yields 57.96 avg. AMOTA. Next is the model without time normalization, where the features include distance between nodes instead of velocity. Despite the time difference still being available in this configuration, we see that explicit time normalization yields an improvement of +5.79 avg. AMOTA, confirming our intuition that encoding relative velocity instead of distance improves tracking by making features invariant to trajectory length. Lastly, we evaluate a model with the commonly-used global Cartesian representation and see that simply switching to our proposed localized polar parametrization gives a significant improvement of +17.55 avg. AMOTA. This validates our intuition that incorporating a domain-appropriate inductive bias improves generalization from scarce data. For completeness, in the supplementary, we provide evaluations of these models trained on the full training set.

Intra-frame connections. *Does spatial context matter?* Tab. 4 shows that adding spatial *intra-frame* edges improves avg. AMOTA by +1.05 and significantly improves recall (+2.4%) at a marginal increase in IDs (+15). For better contextual awareness, we aggregate messages from temporal and spatial edges separately. An ablation study of this technique is in the supplementary material.

Sparse graph construction. *What is the impact of our sparse graph construction on tracking performance?* In Tab. 5 we compare results obtained by models using half (0.5x) and double (2.0x) of the measured maximal velocity values to constrain edges with the ones from our default model (1x). Reducing maximum allowed velocity (0.5x) removes valuable edges that hypothesize valid associations, while permitting higher values (2x) introduces irrelevant edges. In both cases, we observe a significant performance drop across all metrics (recall, precision, AMOTA), due to message passing becoming less complete and noisier and edge classification more challenging. This confirms that our data-driven physics-based sparse graph construction is the optimal approach.

Table 6: Online graph construction analysis (nuScenes validation set)

Track connectivity	IDs ↓ Recall ↑ AMOTA ↑			class-specific AMOTA ↑						
	total	average	average	car	pedestrian	bicycle	bus	motorcycle	trailer	truck
Ours	439	72.46	67.27	81.26	78.79	49.38	82.76	67.19	45.80	65.70
Consecutive	485	69.90	66.03	81.04	77.37	48.84	82.45	66.58	40.66	65.23
Dense	1024	68.58	61.39	71.08	75.20	49.70	79.78	52.03	41.15	60.79

Table 7: CenterPoint (CP) [62] and our method when trained on training data from one city, and evaluated on the validation data from another

Train city → eval city	Tracking model	IDs ↓ total	Recall ↑ average	AMOTA ↑ average	class-specific AMOTA ↑						
					car	ped	bicycle	bus	motor	trailer	truck
Boston → Singapore	Ours	145	64.48	63.12	82.26	72.81	31.49	77.70	43.17	0	71.28
	CP	306	61.02	59.71	79.26	67.47	20.52	78.86	41.13	0	71.04
Singapore → Boston	Ours	104	52.30	50.28	78.60	82.59	36.70	71.22	28.71	11.31	42.83
	CP	314	53.32	47.06	77.01	76.18	34.86	71.07	13.54	13.18	43.55

Evolving online graph connectivity. To validate our proposed approach to online graph connectivity, we present ablation experiments that confirm the advantage of our technique over alternatives discussed in Sec.4.4. As shown in Tab. 6, our experimental results align with our expectations based on the theoretical properties of each option. *Dense* (MPNTrack++) linking (61.39 avg. AMOTA) completely ignores past trajectories and produces the lowest results. Next, *consecutive* (prune inactive) chaining introduces a significant improvement with 66.03 avg. AMOTA. Finally, our proposed *prune + skip* connectivity leads to a significant improvement over both alternatives with 67.27 avg. AMOTA.

5.4 Generalization study

In this section, we show how *PolarMOT* generalizes across geographic locations and datasets. To this end, we (i) use the nuScenes dataset, recorded in Singapore and Boston, to train the model on one city and evaluate on the other and (ii) evaluate our model, trained on nuScenes, on KITTI data without any fine-tuning.

Cross-city generalization: Boston ↔ Singapore. In this cross-city evaluation we compare our method to CenterPoint (we use detections from the corresponding re-trained CenterPoint model). As shown in Tab. 7, our method generalizes significantly better: +3.41 avg. AMOTA on Boston (trained) → Singapore (evaluated) and +3.33 avg. AMOTA on Singapore → Boston. In both cases we also observe a significant improvement in both recall and number of ID-switches. This confirms that our method generalizes very well across regions, which we believe is largely due to our feature parametrization (Sec. 4.3).

Cross-dataset generalization: nuScenes → KITTI. We report our results on the unofficial KITTI 3D MOT benchmark [56] in Tab. 8, and on the official KITTI 2D MOT benchmark in Tab. 9. We *only* evaluate our nuScenes-trained model on KITTI dataset, which we consider an ultimate generalization

Table 8: Unofficial KITTI 3D MOT validation set benchmark [56]. Our model was trained **only** on nuScenes dataset

Method name	3D input	2D input	IDs ↓		sAMOTA ↑		MOTA ↑		Recall ↑	
			car	ped	car	ped	car	ped	car	ped
Ours <i>online</i>	✓	✗	31	9	94.32	94.08	93.93	93.48	94.54	93.66
PC-TCNN [59]	✓	✗	1	–	95.44	–	unpub	–	unpub	–
EagerMOT [17]	✓	✓	2	36	94.94	92.95	96.61	93.14	96.92	93.61
GNN3DMOT [57]	✓	✓	10	–	93.68	–	84.70	–	unpub	–
AB3DMOT [56]	✓	✗	0	1	91.78	73.18	83.35	66.98	92.17	72.82

Table 9: KITTI 2D MOT test set benchmark. Our model was trained **only** on nuScenes dataset

Method name	3D input	2D input	IDs ↓		HOTA ↑		AssA ↑		AssRe ↑		MOTA ↑	
			car	ped	car	ped	car	ped	car	ped	car	ped
Ours <i>online</i>	✓	✗	462	270	75.16	43.59	76.95	48.12	80.00	51.95	85.08	46.98
PC-TCNN [59]	✓	✗	37	–	80.90	–	84.13	–	87.46	–	91.70	–
PermaTrack [54]	✗	✓	258	403	78.03	48.63	78.41	45.61	81.14	49.63	91.33	65.98
PC3T [58]	✓	✗	225	–	77.80	–	81.59	–	84.77	– 5	88.81	–
Mono_3D_KF [45]	✗	✓	162	267	75.47	42.87	77.63	46.31	80.23	52.86	88.48	45.44
EagerMOT [17]	✓	✓	239	496	74.39	39.38	74.16	38.72	76.24	40.98	87.82	49.82
SRK.ODESA [35]	✗	✓	380	511	68.51	50.87	63.08	48.78	65.89	53.45	87.79	68.04
3D-TLSR [37]	✗	✓	–	175	–	46.34	–	51.32	–	54.45	–	53.58
MPNTrack [5]	✗	✓	–	397	–	45.26	–	47.28	–	52.18	–	46.23

experiment, as KITTI dataset was recorded using a different sensor under a different frame rate in a different geographical location (Karlsruhe, Germany). For 2D MOT evaluation we simply project our estimated 3D tracks to the image plane. We note that entries are not directly comparable, as different methods use different input detections. However, we observe our method is on-par with EagerMOT [18], which uses lidar and cameras, and the same set of 3D detections. *PolarMOT* is top-performer on the 3D benchmark and among top-4 on the 2D benchmark, performing consistently well on *car* and *pedestrian* classes.

6 Conclusion

We presented *PolarMOT* for 3D multi-object tracking that solely relies on 3D bounding boxes as input without appearance/shape information. Our key contribution is a GNN that encodes spatial and temporal geometric relations via localized polar coordinates. This parametrization enables us to effectively learn to understand long-range temporal and spatial context via message passing and, solely from object interactions, learn a scene representation suitable for tracking via edge classification. We also propose an online graph construction technique to apply *PolarMOT* to streaming data. Our method establishes a new state-of-the-art on the nuScenes dataset among methods that do not rely on image data and, more importantly, generalizes well across geographic regions and datasets.

Acknowledgments. This research was partially funded by the Humboldt Foundation through the Sofja Kovalevskaja Award.

References

1. Aygün, M., Ošep, A., Weber, M., Maximov, M., Stachniss, C., Behley, J., Leal-Taixé, L.: 4d panoptic lidar segmentation. In: CVPR (2021) [4](#)
2. Bergmann, P., Meinhardt, T., Leal-Taixé, L.: Tracking without bells and whistles. In: ICCV (2019) [3](#)
3. Bernardin, K., Stiefelhagen, R.: Evaluating multiple object tracking performance: The clear mot metrics. *JIVP* **2008**, 1–10 (2008) [11](#)
4. Bewley, A., Ge, Z., Ott, L., Ramos, F., Upcroft, B.: Simple online and realtime tracking. In: ICIIP (2016) [4](#)
5. Braso, G., Leal-Taixé, L.: Learning a neural solver for multiple object tracking. In: CVPR (2020) [2](#), [3](#), [4](#), [6](#), [9](#), [14](#)
6. Brendel, W., Amer, M.R., Todorovic, S.: Multi object tracking as maximum weight independent set. In: CVPR (2011) [3](#)
7. Butt, A.A., Collins, R.T.: Multi-target tracking by lagrangian relaxation to min-cost network flow. In: CVPR (June 2013) [3](#)
8. Caesar, H., Bankiti, V., Lang, A.H., Vora, S., Liong, V.E., Xu, Q., Krishnan, A., Pan, Y., Baldan, G., Beijbom, O.: nuScenes: A multimodal dataset for autonomous driving. In: CVPR (2020) [2](#), [9](#), [10](#), [18](#), [21](#), [22](#)
9. Chiu, H.k., Prioletti, A., Li, J., Bohg, J.: Probabilistic 3d multi-object tracking for autonomous driving. In: ICRA (2021) [1](#), [4](#), [9](#), [21](#)
10. Choi, W.: Near-online multi-target tracking with aggregated local flow descriptor. In: ICCV (2015) [3](#)
11. Dellaert, F., Thorpe, C.: Robust car tracking using kalman filtering and bayesian templates. In: Conference on Intelligent Transportation Systems (1997) [4](#)
12. Frossard, D., Urtasun, R.: End-to-end learning of multi-sensor 3d tracking by detection. ICRA (2018) [4](#)
13. Geiger, A., Lenz, P., Urtasun, R.: Are we ready for autonomous driving? the KITTI vision benchmark suite. In: CVPR (2012) [2](#), [10](#)
14. Gilmer, J., Schoenholz, S.S., Riley, P.F., Vinyals, O., Dahl, G.E.: Neural message passing for quantum chemistry. In: International conference on machine learning. pp. 1263–1272. PMLR (2017) [3](#), [4](#), [6](#)
15. Gori, M., Monfardini, G., Scarselli, F.: A new model for learning in graph domains. In: IJCNN (2005) [3](#)
16. Held, D., Levinson, J., Thrun, S., Savarese, S.: Combining 3d shape, color, and motion for robust anytime tracking. In: RSS (2014) [4](#)
17. Kim, A., Ošep, A., Leal-Taixé, L.: Eagermot: 3d multi-object tracking via sensor fusion. In: ICRA (2021) [4](#), [9](#), [11](#), [14](#), [21](#)
18. Kim, D., Woo, S., Lee, J.Y., Kweon, I.S.: Video panoptic segmentation. In: CVPR (2020) [14](#)
19. Kingma, D.P., Ba, J.: Adam: A method for stochastic optimization. In: ICLR (2015) [10](#)
20. Kuhn, H.W., Yaw, B.: The hungarian method for the assignment problem. *Naval Res. Logist. Quart* pp. 83–97 (1955) [3](#)
21. Lang, A.H., Vora, S., Caesar, H., Zhou, L., Yang, J., Beijbom, O.: Pointpillars: Fast encoders for object detection from point clouds. In: CVPR (2019) [4](#)
22. Leal-Taixé, L., Canton-Ferrer, C., Schindler, K.: Learning by tracking: Siamese cnn for robust target association. CVPR Workshops (2016) [3](#)
23. Leal-Taixé, L., Fenzi, M., Kuznetsova, A., Rosenhahn, B., Savarese, S.: Learning an image-based motion context for multiple people tracking. In: CVPR (2014) [3](#)

24. Leibe, B., Leonardis, A., Schiele, B.: Robust object detection with interleaved categorization and segmentation. *IJCV* **77**(1-3), 259–289 (2008) [3](#)
25. Leibe, B., Schindler, K., Cornelis, N., Gool, L.V.: Coupled object detection and tracking from static cameras and moving vehicles. *PAMI* **30**(10), 1683–1698 (2008) [3](#)
26. Li, J., Gao, X., Jiang, T.: Graph networks for multiple object tracking. In: *WACV* (2020) [9](#)
27. Lin, T.Y., Goyal, P., Girshick, R., He, K., Dollár, P.: Focal loss for dense object detection. In: *ICCV* (2017) [10](#), [18](#)
28. Liu, L., Jiang, H., He, P., Chen, W., Liu, X., Gao, J., Han, J.: On the variance of the adaptive learning rate and beyond. In: *ICLR* (April 2020) [10](#)
29. Loshchilov, I., Hutter, F.: SGDR: stochastic gradient descent with warm restarts. In: *ICLR* (2017) [10](#)
30. Luiten, J., Fischer, T., Leibe, B.: Track to reconstruct and reconstruct to track. *RAL* **5**(2), 1803–1810 (2020) [3](#)
31. Luiten, J., Ošep, A., Dendorfer, P., Torr, P., Geiger, A., Leal-Taixé, L., Leibe, B.: Hota: A higher order metric for evaluating multi-object tracking. *IJCV* (2020) [11](#)
32. Maas, A.L., Hannun, A.Y., Ng, A.Y.: Rectifier nonlinearities improve neural network acoustic models. In: *ICML* (2013) [19](#)
33. Milan, A., Roth, S., Schindler, K.: Continuous energy minimization for multitarget tracking. *PAMI* **36**(1), 58–72 (2014) [3](#)
34. Moosmann, F., Stiller, C.: Joint self-localization and tracking of generic objects in 3d range data. In: *ICRA* (2013) [4](#)
35. Mykheivskyi, D., Borysenko, D., Porokhonskyi, V.: Learning local feature descriptors for multiple object tracking. In: *ACCV* (2020) [14](#)
36. Nair, V., Hinton, G.E.: Rectified linear units improve restricted boltzmann machines. In: *ICML* (2010) [10](#)
37. Nguyen, U., Heipke, C.: 3d pedestrian tracking using local structure constraints. *ISPRS Journal of Photogrammetry and Remote Sensing* **166**, 347–358 (2020) [14](#)
38. Ošep, A., Mehner, W., Mathias, M., Leibe, B.: Combined image- and world-space tracking in traffic scenes. In: *ICRA* (2017) [3](#)
39. Ošep, A., Mehner, W., Voigtlaender, P., Leibe, B.: Track, then decide: Category-agnostic vision-based multi-object tracking. In: *ICRA* (2018) [3](#)
40. Petrovskaya, A., Thrun, S.: Model based vehicle detection and tracking for autonomous urban driving. *AR* **26**, 123–139 (2009) [4](#)
41. Pirsiaavash, H., Ramanan, D., Fowlkes, C.C.: Globally-optimal greedy algorithms for tracking a variable number of objects. In: *CVPR* (2011) [3](#)
42. Qi, C.R., Liu, W., Wu, C., Su, H., Guibas, L.J.: Frustum pointnets for 3d object detection from rgb-d data. In: *CVPR* (2017) [4](#)
43. Qi, C.R., Su, H., Mo, K., Guibas, L.J.: Pointnet: Deep learning on point sets for 3d classification and segmentation. In: *CVPR* (2017) [4](#)
44. Qi, C.R., Yi, L., Su, H., Guibas, L.J.: Pointnet++: Deep hierarchical feature learning on point sets in a metric space. In: *NeurIPS* (2017) [4](#)
45. Reich, A., Wuensche, H.J.: Monocular 3d multi-object tracking with an ekf approach for long-term stable tracks. In: *FUSION* (2021) [14](#)
46. Schulter, S., Vernaza, P., Choi, W., Chandraker, M.K.: Deep network flow for multi-object tracking. In: *CVPR* (2017) [3](#)
47. Sharma, S., Ansari, J.A., Krishna Murthy, J., Madhava Krishna, K.: Beyond pixels: Leveraging geometry and shape cues for online multi-object tracking. In: *ICRA* (2018) [3](#)

48. Shi, S., Wang, X., Li, H.: PointRCNN: 3D Object Proposal Generation and Detection From Point Cloud. In: CVPR (2019) 4
49. Shi, W., Rajkumar, R.: Point-gnn: Graph neural network for 3d object detection in a point cloud. In: CVPR (2020) 11
50. Son, J., Baek, M., Cho, M., Han, B.: Multi-object tracking with quadruplet convolutional neural networks. In: CVPR (2017) 3
51. Tang, S., Andres, B., Andriluka, M., Schiele, B.: Subgraph decomposition for multi-target tracking. In: CVPR (2015) 3
52. Teichman, A., Levinson, J., Thrun, S.: Towards 3D object recognition via classification of arbitrary object tracks. In: ICRA (2011) 4
53. Thomas, H., Qi, C.R., Deschaud, J.E., Marcotegui, B., Goulette, F., Guibas, L.J.: Kpconv: Flexible and deformable convolution for point clouds. In: ICCV (2019) 4
54. Tokmakov, P., Li, J., Burgard, W., Gaidon, A.: Learning to track with object permanence. In: ICCV (2021) 14
55. Voigtlaender, P., Krause, M., Ošep, A., Luiten, J., Sekar, B., Geiger, A., Leibe, B.: MOTS: Multi-object tracking and segmentation. In: CVPR (2019) 3
56. Weng, X., Wang, J., Held, D., Kitani, K.: 3D Multi-Object Tracking: A Baseline and New Evaluation Metrics. In: IROS (2020) 1, 2, 4, 11, 13, 14
57. Weng, X., Wang, Y., Man, Y., Kitani, K.: Gnn3dmot: Graph neural network for 3d multi-object tracking with multi-feature learning. In: CVPR (2020) 1, 4, 14
58. Wu, H., Han, W., Wen, C., Li, X., Wang, C.: 3d multi-object tracking in point clouds based on prediction confidence-guided data association. IEEE TITS (2021) 14
59. Wu, H., Li, Q., Wen, C., Li, X., Fan, X., Wang, C.: Tracklet proposal network for multi-object tracking on point clouds. In: IJCAI (2021) 14
60. Xu, Y., Ošep, A., Ban, Y., Horaud, R., Leal-Taixé, L., Alameda-Pineda, X.: How to train your deep multi-object tracker. In: CVPR (2020) 3
61. Yan, Y., Mao, Y., Li, B.: Second: Sparsely embedded convolutional detection. Sensors 18(10), 3337 (2018) 4
62. Yin, T., Zhou, X., Krähenbühl, P.: Center-based 3d object detection and tracking. In: CVPR (2021) 1, 4, 9, 11, 13, 21, 22
63. Zaech, J.N., Liniger, A., Dai, D., Danelljan, M., Van Gool, L.: Learnable online graph representations for 3d multi-object tracking. IEEE R-AL (2022) 4, 9, 21
64. Zeng, Y., Ma, C., Zhu, M., Fan, Z., Yang, X.: Cross-modal 3d object detection and tracking for auto-driving. In: IROS (2021) 1, 4, 9
65. Zhang, L., Yuan, L., Nevatia, R.: Global data association for multi-object tracking using network flows. In: CVPR (2008) 3
66. Zhou, X., Koltun, V., Krähenbühl, P.: Tracking objects as points. In: ECCV (2020) 3
67. Zhou, Y., Tuzel, O.: Voxelnet: End-to-end learning for point cloud based 3d object detection. In: CVPR (2018) 4

PolarMOT: How far can geometric relations take us in 3D multi-object tracking?

Supplementary Material

A Implementation details

A.1 Training and augmentation

Training. As training data we use annotated training keyframes from the nuScenes [8] dataset. We represent labeled boxes as nodes in the graph. Edges in the graph are labeled positive if they connect nodes with the same track ID (across any number of frames) and negative otherwise. During model training, all input clips are processed individually and each edge is considered an independent sample that contributes to the total focal loss [27].

Data augmentation. To mimic noisy, real-world detectors, we rely on data augmentation. We add random bounding box detections at each frame before the graph construction to imitate false positive detections. For each frame, the number of added boxes is a fraction of the number of real boxes (between 0.7 and 0.9 for each class) plus a fixed number (between 1 and 3) to augment completely empty frames. Pose coordinates (position and orientation) of augmented boxes are sampled from uniform distributions whose parameters are the minimum and maximum values of corresponding coordinates to labeled boxes.

We also augment input graphs at each training iteration. To mimic occlusions and miss-classifications, we randomly drop nodes (between 40%-60%) at each frame as well as some complete frames from our graphs. To emulate imprecise detections, we further perturb each initial edge feature, representing differences in object poses, with noise vectors sampled from class-specific Gaussian distributions with zero mean. For each class, the standard deviation for distributions of distance noise (meters) is between 0.05 and 0.35, for polar angle noise (radians) between 0.1 and 0.25, and for orientation noise (radians) between 0.05 and 0.25. For further augmentation, we fully remove approximately 20% of all edges in the graph. These augmentations ensure that our model is robust to imperfect/noisy inputs that we obtain from real-world 3D object detectors.

Inference. In multi-object tracking, track IDs need to be distinct at each frame, *i.e.*, only one object detection can be assigned to each identity (track ID). In our problem setting, this means that every node in the graph can have at most one positive edge connecting it to each past and future frame. We do not impose this constraint on *PolarMOT* during the training (*i.e.*, we train our model as an unconstrained binary classifier). However, we do ensure this constraint during inference via a simple post-processing procedure.

In particular, given edge classification scores from our model, edges with a score higher than a certain threshold (between 0.5 and 0.8 for each class) are

Table 10: Neural network architecture of *PolarMOT*. Each cell describes the output dimensionality of each layer in the fully-connected MLPs of our model

	Edge initial	Node initial	Edge model	Edge pres, past, fut	Node model	Final edge classifier
Input	4	48	80	80	96	16
1st layer output	16	64	64	64	128	64
2nd layer output	16	128	16	32	64	32
3rd layer output		32			32	16
4th layer output						1

positive, others are negative. Then, positive edge labels are *greedily* assigned starting from the highest score. As soon as a positive edge is assigned between nodes o_i^k and o_j^m at frames k and m , all other edges between node o_i^k and frame m (and between node o_j^m and frame k) are ignored from further assignment. This greedy procedure ensures that positive edges with the highest confidence are assigned first and each node has at most one positive edge to each frame.

A.2 Network structure

In this section, we detail the architecture of our network, explained in Sec. 4.2 in the main paper. In Tab. 10, we outline our network architecture composed entirely of multi-layer perceptrons (MLPs) with fully-connected layers. For each MLP, we list the dimensionality of all of its layers: input, intermediary and output. Here, “Edge initial” and “Node initial” columns correspond to MLP_{edge_init} and MLP_{node_init} (Eq. 4 and 5 in the paper), which produce initial learned embeddings from the initial relative features. The “Edge model” column describes MLP_{edge} (Eq. 1 in the paper) that processes edge features at each message passing step. The columns “Edge pres., past&fut.” describe the identical composition of MLP_{pres} and $\text{MLP}_{past}/\text{MLP}_{fut}$, which process *intra-frame* edges and two temporal directions of *inter-frame* edges (Eq. 2 in the paper). The “Node model” column outlines MLP_{node} that aggregates all edge embeddings and produces node features at each step (Eq. 3 in the paper). Finally, the last column denotes the structure of the MLP used to classify edges based on the latest edge embeddings. We use leaky ReLU [32] between all layers of the network.

In our experiments, we always perform $L = 4$ message passing steps. For offline inference, we process clips of 11 frames and for online tracking, we keep only the 3 latest detections for each track history.

B Experimental evaluation

B.1 Edge parametrization ablation on the full training set

In the main paper, we ablated the impact of our proposed feature representation (time-normalized localized polar coordinates) by comparing models trained on the official nuScenes mini split. The main advantage of our representation is the

Table 11: Ablation on parametrization of geometric relations among objects on the nuScenes validation set. Trained on the **full** training set

Localized polar	Normalized by time	IDs ↓ total	Recall ↑ average	AMOTA ↑ average	class-specific AMOTA ↑						
					car	ped	bicycle	bus	motor	trailer	truck
✓	✓	213	75.14	71.14	85.83	81.70	54.10	87.36	72.32	48.67	68.03
✓	✗	182	72.85	70.27	86.12	81.70	51.73	87.79	69.29	47.20	68.07
✗	✓	225	70.90	69.75	85.89	81.72	48.92	87.54	69.25	47.60	67.31

Table 12: Ablation on the impact of contextual aggregation in node updates on the nuScenes validation set

Node aggregation connections	IDs ↓ total	Recall ↑ average	AMOTA ↑ average	class-specific AMOTA ↑						
				car	ped	bicycle	bus	motor	trailer	truck
Past/Present/Future	213	75.14	71.14	85.83	81.70	54.10	87.36	72.32	48.67	68.03
Spatial/Temporal	968	60.29	55.83	81.48	77.46	48.76	61.09	30.23	29.22	62.56
All together	765	26.75	23.30	0	72.56	40.75	19.80	0	0	30.04

inductive bias, which helps the model better understand long trajectories, turns and non-holonomic motion in general. The benefits of this inductive bias are best demonstrated when the amount of training data is low, which is why we used the mini split in our ablation.

For completeness, in Tab. 11, we provide the same ablation when the full training set is used. Unsurprisingly, with enough data (*e.g.* car, pedestrian and bus classes), different feature representations perform similarly because there are enough samples to learn motion bias directly from data. On the other hand, for rarely-observed classes, such as bicycles, motorcycles and trailers, using a better feature representation is clearly beneficial, *e.g.* *bicycle* AMOTA rises from 48.92 to 54.10. This aligns with our main ablation results, where our parametrization outperforms standard representation in low data regimes.

B.2 Contextual node aggregation

During message passing, our node aggregation step processes messages from **past**, **present** and **future** separately to maintain contextual awareness. To ablate the importance of this technique, we evaluate 3 versions of our trained model with different aggregation logic and show the results in Tab. 12.

When both **temporal** messages (past and future) are aggregated together, the model loses its time-awareness and its tracking performance significantly declines -15.31 avg. AMOTA (from 71.14 down to 55.83). Moreover, if **spatial** messages are also aggregated in the same single group, the model is completely unaware of scene context and geometric scene composition, so its avg. AMOTA falls further by -32.53 (a total decline of 47.84 from our default contextual aggregation).

Table 13: CenterPoint (CP) [62] and our method when trained and evaluating only on one city

Train city → eval city	Tracking model	IDs ↓ total	Recall ↑ average	AMOTA ↑ average	class-specific AMOTA ↑						
					car	ped	bicycle	bus	motor	trailer	truck
Singapore → Singapore	Ours	145	77.82	75.79	85.42	77.17	51.41	85.76	74.23	0	80.73
	CP	351	72.97	70.22	82.66	71.97	39.71	85.17	62.36	0	79.44
Boston → Boston	Ours	48	70.94	70.17	85.80	85.16	58.57	83.45	60.89	52.75	64.58
	CP	246	67.78	65.96	83.54	81.37	50.00	82.47	51.63	48.61	64.10

Table 14: Extended results of state-of-the-art methods for 3D multi-object tracking on the NuScenes test set benchmark. Legend: L – lidar, P – ego poses, B – 3D boxes

Method name	Input modality	MT ↑	ML ↓	Frag ↓	TID ↓	LGD ↓
		total	total	total	average	average
Ours	3D (B)	5701	1686	332	0.444	0.657
OGR3MOT [63]	3D (B + P)	5278	2094	371	0.575	0.782
CenterPoint [62]	3D (L + P)	5399	1818	553	0.415	0.720
IPRL-TRI [9]	3D (B + P)	4294	2184	776	0.960	1.376
AlphaTrack[63]	3D + 2D + P	5560	1744	480	0.409	0.755
EagerMOT [17]	3D + 2D + P	5303	1842	601	0.448	0.801

B.3 Cross-city generalization oracle results

In the main paper, we demonstrated the ability of our model to generalize across different cities by training it in Boston and evaluating in Singapore (and vice versa). To provide a better baseline and show how well the model would normally perform in each of the cities, we present Tab. 13 where models are trained and evaluated on the same single city, *i.e.* only Boston or only Singapore.

Since *PolarMOT* demonstrates better performance than CenterPoint [62] on the full nuScenes [8] validation set (see Tab. 2 in the main paper), it is unsurprising that its results on individual cities are also better.

B.4 Extended evaluation results

In this section, we present extended versions of the experimental evaluations detailed in the main paper. These tables include additional tracking metrics reported by the nuScenes benchmark [8], which we provide for completeness:

- MT (*mostly tracked*): percentage of tracks tracked correctly for at least 80% of their life span
- ML (*mostly lost*) percentage of tracks tracked correctly for at most 20% of their life span
- Frag. (*fragmentations*): the number of times a trajectory is interrupted during tracking.
- TID (*track initialization in seconds*): time until the first detection of the track is successfully tracked.

Table 15: Extended results for online vs. offline tracking on the nuScenes val set [8]

Method name	Input modality	MT \uparrow total	ML \uparrow total	Frag \downarrow total	TID \downarrow average	LGD \downarrow average
Ours <i>offl.</i>	3D	4524	1452	332	0.379	0.672
Ours <i>onl.</i>	3D	4262	1545	285	0.636	0.901
CenterPoint <i>onl.</i>	3D	4405	1508	445	0.516	0.956

Table 16: Extended results for CenterPoint (CP) [62] and our method when trained on training data from one city, and evaluated on the validation data from another

Train city \rightarrow eval city	Tracking model	MT \uparrow total	ML \downarrow total	Frag \downarrow total	TID \downarrow average	LGD \downarrow average
Boston \rightarrow Singapore	Ours	1595	765	139	0.461	0.773
	CP	1464	861	224	0.584	1.037
Singapore \rightarrow Boston	Ours	2274	1177	147	0.850	1.171
	CP	2282	1147	253	0.715	1.209

- LGD (*longest gap duration in seconds*): time an object instance has been incorrectly tracked.

In Tab. 14 we show extended results on the nuScenes test set benchmark (Tab. 9 in the main paper).

Tab. 15 extends Tab. 2 in the main paper and details offline and online model evaluations on the nuScenes validation set.

Tab. 16 extends Tab. 7 in the main paper where *PolarMOT* and CenterPoint [62] are trained on one city and evaluated on the other. For evaluations of our method, we use detections produced by the corresponding CP model to make sure each pair of trackers uses the same set of detections.

These extended evaluations along with our code, models and experimental data are available at [polar-mot.github.io](https://github.com/polar-mot).